nature communications

Article

https://doi.org/10.1038/s41467-024-53483-z

Optimizing the reaction pathway of methane photo-oxidation over single copper sites

Received: 21 May 2024

Accepted: 14 October 2024

Chengyang Feng[1,2], Shouwei Zuo[1,2], Miao Hu[1,2], Yuanfu Ren[1,2], Liwei Xia[3], Jun Luo[4], Chen Zou[1,2], Sibo Wang[5], Yihan Zhu[3], Magnus Rueping[2], Yu Han[6] & Huabin Zhang[1,2] ✉

Direct photocatalytic conversion of methane to value-added C_1 oxygenate with O_2 is of great interest but presents a significant challenge in achieving highly selective product formation. Herein, a general strategy for the construction of copper single-atom catalysts with a well-defined coordination microenvironment is developed on the basis of metal-organic framework for selective photo-oxidation of CH_4 to HCHO. We propose the directional activation of O_2 on the mono-copper site breaks the original equilibrium and tilts the balance of radical formation almost completely toward •OOH. The synchronously generated •OOH and $\bullet CH_3$ radicals rapidly combine to form HCHO while inhibiting competing reactions, thus resulting in ultra-highly selective HCHO production (nearly 100%) with a time yield of 2.75 mmol g_{cat}^{-1} h^{-1}. This work highlights the potential of rationally designing reaction sites to manipulate reaction pathways and achieve selective CH_4 photo-oxidation, and could guide the further design of high-performance single-atom catalysts to meet future demand.

Methane (CH_4) comprises 70–90% of natural gas and is widely recognized as an essential feedstock in the manufacturing of chemicals[1–4]. However, due to the intense bond energy (439 kJ mol^{-1}) and the weak polarization of carbon-hydrogen (C−H) bonds in methane, selective conversion of methane remains a significant challenge[5,6]. Currently, the steam reforming reaction serves as the primary approach for transforming methane into syngas. Unfortunately, this method requires extreme temperatures (>800 °C) and pressures (>30 bar), thereby hindering its application in sustainable development[7–9]. Therefore, it becomes imperative to explore strategies that enable the conversion of methane to value-added products under mild conditions[10,11]. Recently, photocatalytic oxidation of CH_4 to HCHO or CH_3OH under room temperature and mild pressure is considered to be one of the “holy grails” in C_1 chemistry, but suffers from the challenge to control the reaction pathway and product selectivity[12,13].

During the CH_4 photo-oxidation, O_2 and CH_4 undergo initial activation into free radicals with subsequently combining. It is known that the CH_4 oxidation process involves multiple free radicals ($\bullet CH_3$, •OOH, and •OH) to produce a wide variety of products, such as HCHO and CH_3OH, as well as overoxidized CO_2, while the distribution of final products is determined by the O_2 activation and oxygen radical species[14,15].

$$\bullet OOH(aq) + CH_3(aq) \rightarrow CH_3OOH(aq) \rightarrow HCHO(aq) + H_2O(l) \quad (1)$$

---

[1]Center for Renewable Energy and Storage Technologies (CREST), Physical Science and Engineering Division, King Abdullah University of Science and Technology, Thuwal, Saudi Arabia. [2]KAUST Catalysis Center (KCC), Division of Physical Science and Engineering, King Abdullah University of Science and Technology (KAUST), Thuwal, Saudi Arabia. [3]Center for Electron Microscopy, Institute for Frontier and Interdisciplinary Sciences, State Key Laboratory Breeding Base of Green Chemistry Synthesis Technology and College of Chemical Engineering, Zhejiang University of Technology, Hangzhou, Zhejiang, China. [4]State Key Laboratory of Featured Metal Materials and Life-cycle Safety for Composite Structures, MOE Key Laboratory of New Processing Technology for Nonferrous Metals and Materials, and School of Resources, Environment and Materials, Guangxi University, Nanning, China. [5]State Key Laboratory of Photocatalysis on Energy and Environment, College of Chemistry, Fuzhou University, Fuzhou, China. [6]Electron Microscopy Center, South China University of Technology, Guangzhou, China. ✉e-mail: huabin.zhang@kaust.edu.sa

$$\bullet\text{OH(aq)} + \bullet\text{CH}_3\text{(aq)} \rightarrow \text{CH}_3\text{OH(aq)} \tag{2}$$

However, random reaction sites on the surface of traditional photocatalysts lead to the generation of series oxygen radicals, and the overly oxidizing nature of •OH frequently results in multi-step oxidation or even over-oxidation of the product, thus influencing selectivity[16–18]. Hence, strategically managing the O_2 activation process to produce •OOH is advisable for achieving a highly selective HCHO synthesis[19,20]. Depending on the competitiveness of the reaction, constructing highly active and selective reaction sites on the surface of randomly positioned catalysts can significantly break the balance between the main reaction and the competing reactions (Supplementary Fig. 1). If the activity gap between the active site and the random site is sufficiently significant, the competitive equilibrium will continuously shift towards the main reaction, ultimately resulting in the near-complete suppression of the competitive reaction. Under this guidance, manipulating the mono-metal site is expected to achieve selectivity in the activation of O_2 to •OOH, benefiting from the end-on O_2 adsorption on it to minimize O-O bond breaking (Supplementary Fig. 2). Hence, to achieve high efficiency and selectivity for CH_4 photo-oxidation, it is crucial to construct single-atom catalysts with well-defined reaction microenvironments to control the types of active free radicals, which put forward higher requirements for the precise design of photocatalysts.

Metal-organic frameworks (MOFs) constructed from secondary building units of metal clusters and organic linkers provide a tunable platform for the locally precise design of photocatalysts[21–24]. Metalizing the hydroxyl groups (μ_3-OH) on the $[Zr_6(\mu_3\text{-}O)_4(\mu_3\text{-}OH)_4]$ cluster (Zr_6) in Zr-MOF is expected to obtain single-atom sites with clear structures, which allow precisely control of O_2 activation process[25], thereby achieving highly selective CH_4 photo-oxidation. Herein, we support well-defined Cu active sites on deprotonated Zr_6 connecting nodes in the UIO66-NH_2. The pores in MOFs act as microreactors, where O_2 and CH_4 can be activated on the Zr_6 connecting node and organic linkers, respectively. Crucially, the entirely coordinated Zr in the Zr-MOF leads to a deficiency in O_2 adsorption sites, making the introduced mono-copper site serve as the primary effective O_2 activation site (Supplementary Fig. 3), significantly expediting the formation of •OOH while impeding the production of •OH. By employing meticulously designed in-situ spectroscopy and theoretical simulations, we illustrate that the mono-copper site significantly enhances the transformation of O_2 to •OOH, resulting in nearly 100% selectivity towards HCHO in the photo-oxidation of CH_4. In addition, since the reaction is confined in the porous microreactor, the steric confinement of the active species and the ultrafast local mass transfer efficiency greatly enhance the reactivity. In the judicious designed reactive microenvironment, an exceptional time yield of 2.75 mmol g_{cat}^{-1} h^{-1} for the production of HCHO from CH_4 can be achieved.

Results

Synthesis and characterizations

UIO66-NH_2 (UION) is synthesized via a solvothermal reaction between $ZrCl_4$ and 2-Aminoterephthalic acid (H_2ATA) in a mixture of acetic acid and DMF (1:10 v/v) at 120 °C for 12 h (Fig. 1a)[26,27]. The UION is then treated with *n*-BuLi to deprotonate the μ_3-OH at its Zr_6 node, followed by metallization with $CuCl_2$ in THF at room temperature to obtain UION-Cu(Cl) with node-supported copper chloride. The deprotonation is confirmed by the disappearance of the vibrational bands of μ_3-OH (3679 cm^{-1}) in the Fourier transform infrared (FTIR) spectrum (Supplementary Fig. 4). Subsequently, the coordination environment of the mono-copper site is adjusted from -Cu(Cl) to -Cu(OH), which facilitates the initiation of the O_2 reduction reaction (Fig. 1b). The XRD patterns of UION, UION-Cu(Cl) and UION-Cu(OH) are similar to that of pristine UIO as well as simulated UION-Cu(OH) MOF, confirming the retention of UIO-type structure constructed from Zr_6 nodes and H_2ATA linkers (Supplementary Fig. 5). Scanning electron microscopy (SEM) and transmission electron microscopy (TEM) further confirmed that the modification process will not destroy the morphology and crystal form of UION-Cu(OH), and no agglomerated Cu species can be observed (Supplementary Figs. 6–10). Considering the electron beam sensitive characteristics of MOF materials, the low-dose high-angle annular dark-field-scanning transmission electron microscopy (HAADF-STEM) images of samples have been collected to further character the structure information. Figure 1c illustrates the regularly arranged Zr_6 clusters in UION-Cu(OH), which were consistent with the simulated results (Fig. 1d, e). Moreover, the high contrast spots of UION-Cu(OH) match well with the high-resolution structure of UION (Supplementary Fig. 11), implying that Cu species are uniformly distributed on Zr_6 clusters. Energy dispersive X-ray spectroscopy (EDX) mapping further indicates the uniform distribution of Cu throughout the UION-Cu(OH) particles (Fig. 1f).

The Cu loading content is determined by inductively coupled plasma mass spectrometry (ICP-MS) to be 3.48 Cu per Zr_6 node, corresponding to complete metallation of four μ_3-OH sites (Supplementary Table 1). Nitrogen adsorption experiments give a Brunauer-Emmett-Teller surface area of 414.9 $m^2\,g^{-1}$ for UION-Cu(OH), which is smaller than that of the unmetallated UION sample (763.7 $m^2\,g^{-1}$), as expected (Supplementary Fig. 12 and Table 2). The X-ray photoelectron spectroscopy (XPS) of UION-Cu(Cl) and UION-Cu(OH) displays binding energy peaks for Cu $2p_{3/2}$ and $2p_{1/2}$ along with satellite peaks (Supplementary Figs. 13 and 14), indicating that the oxidation state of Cu is +2[22]. The +2 oxidation state of Cu species is also assigned by Cu LMM spectra (Supplementary Fig. 15), which shows characteristic peaks at 572.5 eV[28]. Moreover, electron paramagnetic resonance (EPR) of UION-Cu(OH) exhibits two signals at $g = 2.003$ and $g = 2.320$, respectively (Fig. 2a). The Lorentzian EPR signal at $g = 2.003$ can be assigned to the intrinsic signal of MOF, which is also observed on UIO and UION[29]. The additional hyperfine peak assigned to the hybridized Cu^{II} species is observed at $g = 2.320$, further demonstrating the highly dispersed copper species (Cu^{II})[30,31].

The local coordination environments of mono-copper site in prepared samples have been probed by X-ray absorption fine structure (XAFS) spectra at the Cu K edge. The rising edge at 8985.5 eV in the X-ray absorption near edge structure (XANES) is assigned to the 1s→4p transition of Cu^{II} (Fig. 2b)[32]. The k^2-weighted Fourier transform EXAFS spectra of UION-Cu(Cl) and UION-Cu(OH) exhibit only one peak at around 1.53 Å, with no Cu−Cu (2.23 Å) or Cu-O-Cu (2.54 Å) observed, suggesting that the Cu species are atomically anchored (Fig. 2d). To achieve enhanced resolution in both R and k spaces, an exhaustive wavelet transform (WT) analysis of Cu K-edge EXAFS oscillations has been conducted. As depicted in Fig. 2c, no discernible extended Cu-Cu and Cu-O-Cu features are evident in either UION-Cu(Cl) or UION-Cu(OH), providing additional confirmation of the atomic dispersion of Cu species (Supplementary Fig. 16). The EXAFS spectra are fitted within the 1.0–3.0 Å range based on the density functional theory (DFT) optimized structure model, extracting coordination details for the first shell. The Cu site in UION-Cu(Cl) is stabilized by three oxygens on the Zr_6 cluster and connected to a Cl atom with a Cu-Cl bond length of 2.18 Å (Supplementary Fig. 17 and Supplementary Table 3). In UION-Cu(OH), the Cl atom is substituted by OH, resulting in a four-oxygen coordination environment for Cu. This coordination involves three Cu-O bonds with oxygen atoms at a distance of 1.94 Å and one Cu-O bond with an oxygen atom at a distance of 1.97 Å originating from the -OH group (Fig. 2e and Supplementary Table 3). The preceding results clarify the coordination structure of the mono-copper site and lay the groundwork for investigating the reaction mechanism.

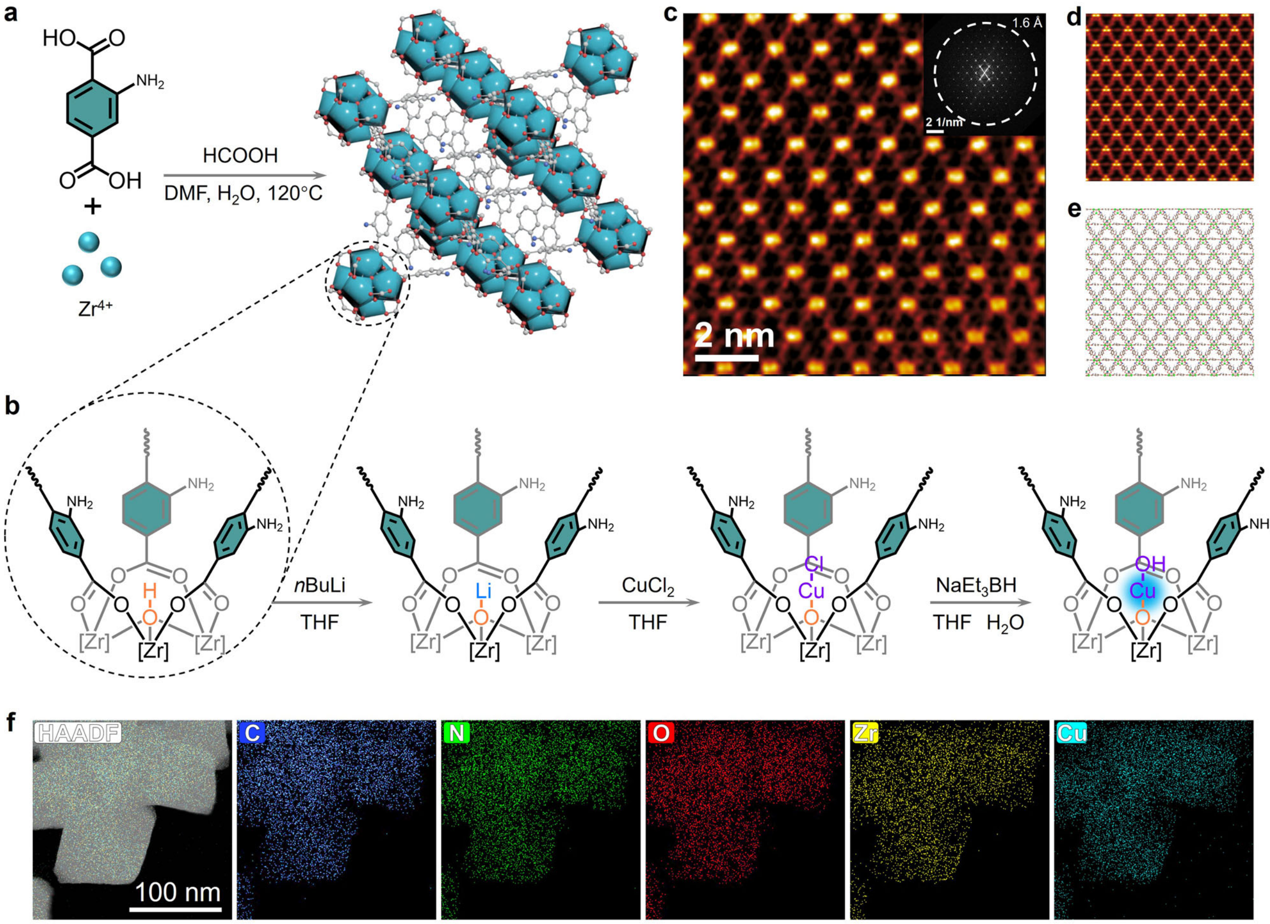

Fig. 1 | Synthesis and characterization of UION-Cu(OH). **a**, **b** Synthetic scheme of the UION-Cu(OH) catalyst (**a**) and illustration of the μ$_3$-OH site in UION for Cu loading to form mono-copper hydroxyl site (**b**). **c** HAADF-STEM image of UION-Cu(OH), inset: FFT of the image with scale bar of 1/nm. **d** Simulated HAADF-STEM image of UION-Cu(OH). **e** Crystal structure of UION-Cu(OH) along [100] direction. **f** STEM-EDXS elemental maps of UION-Cu(OH).

Photocatalytic performance

The photocatalytic performance is assessed through methane conversion in a top-irradiation high-pressure batch reactor, in which 5 mg of photocatalysts are suspended in 20 mL of distilled water in a mixture of 9 bar CH_4 and 1 bar O_2 and subjected to a 5-h irradiation period at 20 °C (Supplementary Fig. 18). Figure 3a present the oxygenates production including HCHO and CH_3OH together with overoxidized CO_2 over prepared photocatalysts. UIO exhibits trace yields of C_1 oxygenates in the reaction, consistent with its limited light absorption and severe charge recombination. UION and UION-Cu(Cl) demonstrate increased production of C_1 oxygenates, yet the resultant products lack selectivity. After adjusting the coordination environment of the mono-copper site into -Cu(OH), there is a substantial enhancement in selectivity, with the target product HCHO reaching almost 100%. The highest HCHO yield is attained at 13.76 mmol g^{-1} over UION-Cu(OH)-3.48, at which point the Cu site is approaching saturation. This outperforms most state-of-the-art photocatalysts operating at similar conditions or even higher pressure (Fig. 3b)[6,16,33–36]. The ultra-high selectivity of the product is further confirmed through NMR ^{1}H and ^{13}C spectra, only $HOCH_2OH$ (the major species in aqueous solutions of HCHO) can be detected over UION-Cu(OH) (Fig. 3c, d). It is important to note that due to the uncontrolled self-conversion of CH_3OOH to HCHO in the product, we quantified HCHO only after CH_3OOH was completely converted to enhance accuracy (Fig. 3c, with no CH_3OOH in the ^{1}H NMR spectrum). To detect the unstable intermediate species CH_3OOH, the reaction solution was stored at low temperature and subjected to NMR testing as soon as possible. The characteristic signal of CH_3OOH was observed at 3.68 ppm, providing clear evidence of CH_3OOH formation (Supplementary Fig. 19). In addition, when the reaction time is extended to 10 h (Fig. 3e), the yield of HCHO increased linearly, while the selectivity remained almost unchanged. Under visible light irradiation, UION-Cu(OH) maintains its high efficiency in converting CH_4 to HCHO, underscoring its excellent catalytic activity (Supplementary Fig. 20).

The catalytic performance under varied conditions is investigated with the absence of catalyst, light, CH_4, and O_2, respectively (Fig. 3f). In all these cases no C_1 oxygenates could be detected, thus confirming that the reaction is a photocatalytic CH_4 oxidation process driven by UION-Cu(OH). Remarkably, in the absence of solvent (H_2O) within the system, CH_4 undergoes over-oxidation to CO_2. This underscores the significance of the free radical reaction process in the liquid phase as a crucial factor in preventing over-oxidation. Furthermore, the isotope-labeling experiments are conducted to verify that HCHO is indeed produced via photocatalytic CH_4 oxidation. As shown in Fig. 3g, the $H^{13}CHO$ and $HCH^{18}O$ peaks prove that the product is derived from CH_4 and O_2. The control experiment in D_2O demonstrates that the solvent does not participate directly in the reaction, it merely serves as a medium for the generation and transfer of free radicals (Supplementary Fig. 21). Notably, a high apparent quantum yield (AQY) of 3.52% at 375 nm has been achieved on UION-Cu(OH), and the calculated AQY at 400, 420, and 450 nm are 1.26%, 0.83%, and 0.22%, respectively, which resembles well with the UV-vis absorption (Fig. 3h).

To investigate the stability of the optimized photocatalyst, the cycling test experiment is carried out over UION-Cu(OH) photocatalyst

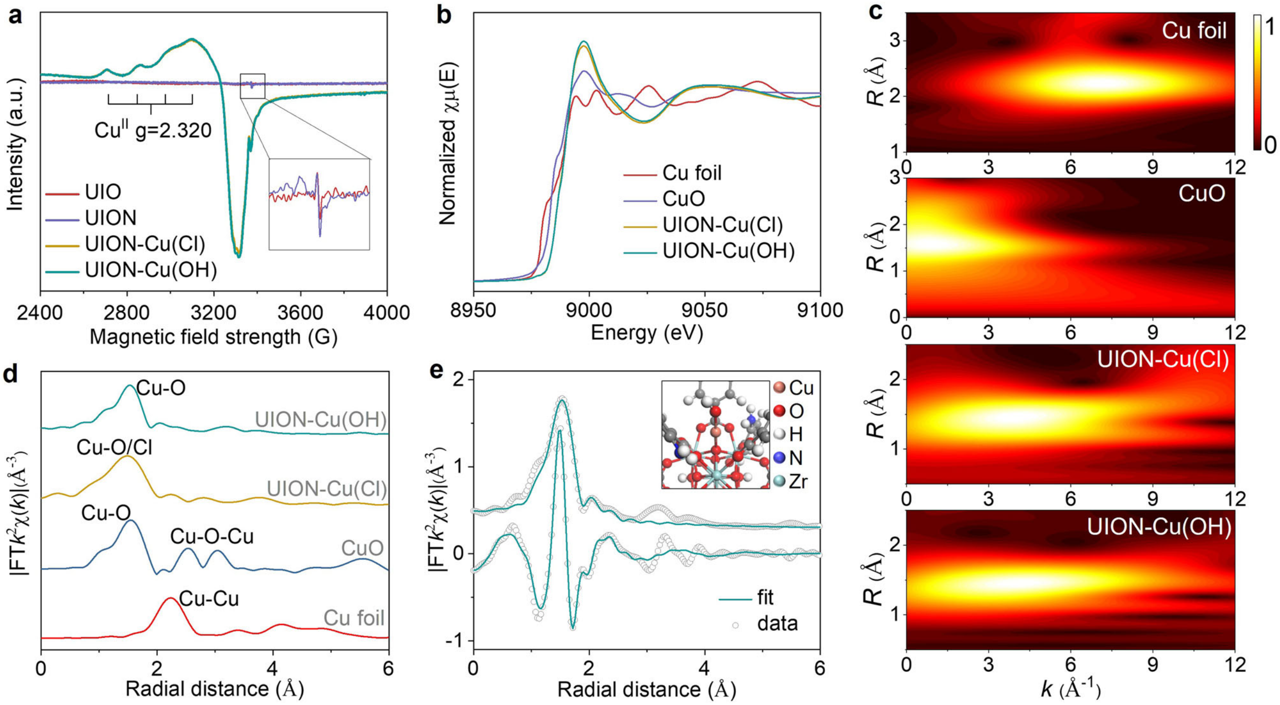

Fig. 2 | Fine structure of mono-copper sites. a EPR spectra of UIO, UION UION-Cu(Cl) and UION-Cu(OH). **b** Cu K-edge XANES experimental spectra of UION-Cu(OH), UION-Cu(Cl), CuO and Cu foil. **c** WT for the k^2-weighted EXAFS signal of Cu foil, CuO,UION-Cu(Cl) and UION-Cu(OH). **d** Fourier-transformed EXAFS spectra of UION-Cu(OH), UION-Cu(Cl), CuO and Cu foil. **e** Fitting of the EXAFS data of UION-Cu(OH) based on the model obtained from DFT simulation.

(Fig. 3i). No obvious decrease of oxygenate yield and selectivity can be observed under 25 h reaction (five cycles), demonstrating the good stability of UION-Cu(OH). Meanwhile, the XRD, XPS, TEM, and XAFS comparison of the used UION-Cu(OH) is carried out (Supplementary Figs. 22–25). These characterizations of UION-Cu(OH) after reaction remain almost the same as the fresh samples, confirming the stable topology of catalyst. Nitrogen adsorption experiment has confirmed that the pore structure of the catalyst remained unblocked even after undergoing multiple runs (Supplementary Fig. 26 and Table S2). In addition to its stable structure, the used catalyst does not exhibit significant carbon deposition or other adsorbed species, which ensures the activity of the mono-copper site (Supplementary Fig. 27).

Charge excitation and migration properties

The optical absorption ability of prepared samples is first inspected by UV-vis diffuse reflectance spectroscopy (DRS). As shown in Fig. 4a, the absorption in UIO is induced by O to Zr charge transfer in Zr_6 inorganic clusters. However, the introduction of amino functional groups initiates an additional charge transfer from the linker to the Zr_6 node, corresponding to strong light absorption in the visible region, indicating superb spatial separation of photogenerated carriers between the linker and node[27,37]. According to the Tauc-plot curves, the mono-copper sites further induce a subtle red shift in the bandgap (Supplementary Fig. 28), implying that these sites optimize the photoexcitation process. To understand the role of mono-copper sites in photocatalytic reaction, the photoelectric properties and kinetic pathways of photocarriers are systematically investigated. The photoluminescence (PL) spectra of the samples are performed to study the separation of photogenerated charge carriers (Supplementary Fig. 29). An intensive PL emission peak at 400-500 nm is detected over the bare UION samples, which is remarkably decreased after the introduction of mono-copper sites, indicating that Cu species favorably prevents the recombination of charge carriers generated on UION MOFs. The time-resolved PL (TRPL) spectra illustrate the dynamic changes in charge transfer induced by the Cu sites. The UION-Cu(OH) sample exhibits the longest fluorescence decay lifetime, corresponding to its optimal photoinduced charge carrier separation efficiency (Supplementary Fig. 30). Furthermore, the photocurrent density increases after the introduction of mono-copper sites, further confirming the enhancement of photoelectron separation and migration (Supplementary Fig. 31b). Similarly, the charge migration improvement is also demonstrated by electrochemical impedance spectroscopy analysis. Nyquist plots (Supplementary Fig. 31a) show a smaller impedance radius of UION-Cu(OH) compared to the bare UION samples, demonstrating the superior separation and transport of photoinduced charges in UION-Cu(OH), which accounts well for its superior photocatalytic activity[38].

To thoroughly clarify the regulation of transient photoelectron transfer kinetics facilitated by mono-copper sites, femtosecond transient absorption (fs-TA) measurements are conducted. As illustrated in Fig. 4b, c, the fs-TA spectra of bare UION and UION-Cu(OH) are presented in the 390–690 nm region. Evidently, the fs-TA spectra of UION and UION-Cu are primarily characterized by a photoinduced absorption (PA) signal centered at 625 nm, which can be ascribed to the secondary light absorption by excited state electrons. The PA signal intensifies as photogenerated electrons accumulate in the conduction band and subsequently diminishes as a result of recombination between photogenerated electrons and holes (Supplementary Fig. 32). Therefore, by fitting the decay process of the PA signal, the kinetic behavior of photogenerated carrier recombination can be obtained. As shown in Fig. 4d, e, the kinetic plots with typical fitting curves illustrate the decay of both UION and UION-Cu(OH) followed a biexponential model, exhibiting one fast component (τ_1) with time constants of 17.87 and 23.10 ps, respectively, as well as a slower component (τ_2) with a time constant extending to 183.2 and 400.4 ps. The noteworthy increase in both τ_1 (charge-carrier trapping) and τ_2 (excitonic recombination) lifetime suggests that the mono-copper species can serve as electron storage sites, which can facilitate the extraction of photoexcited electron and delay the recombination of excited state electrons.

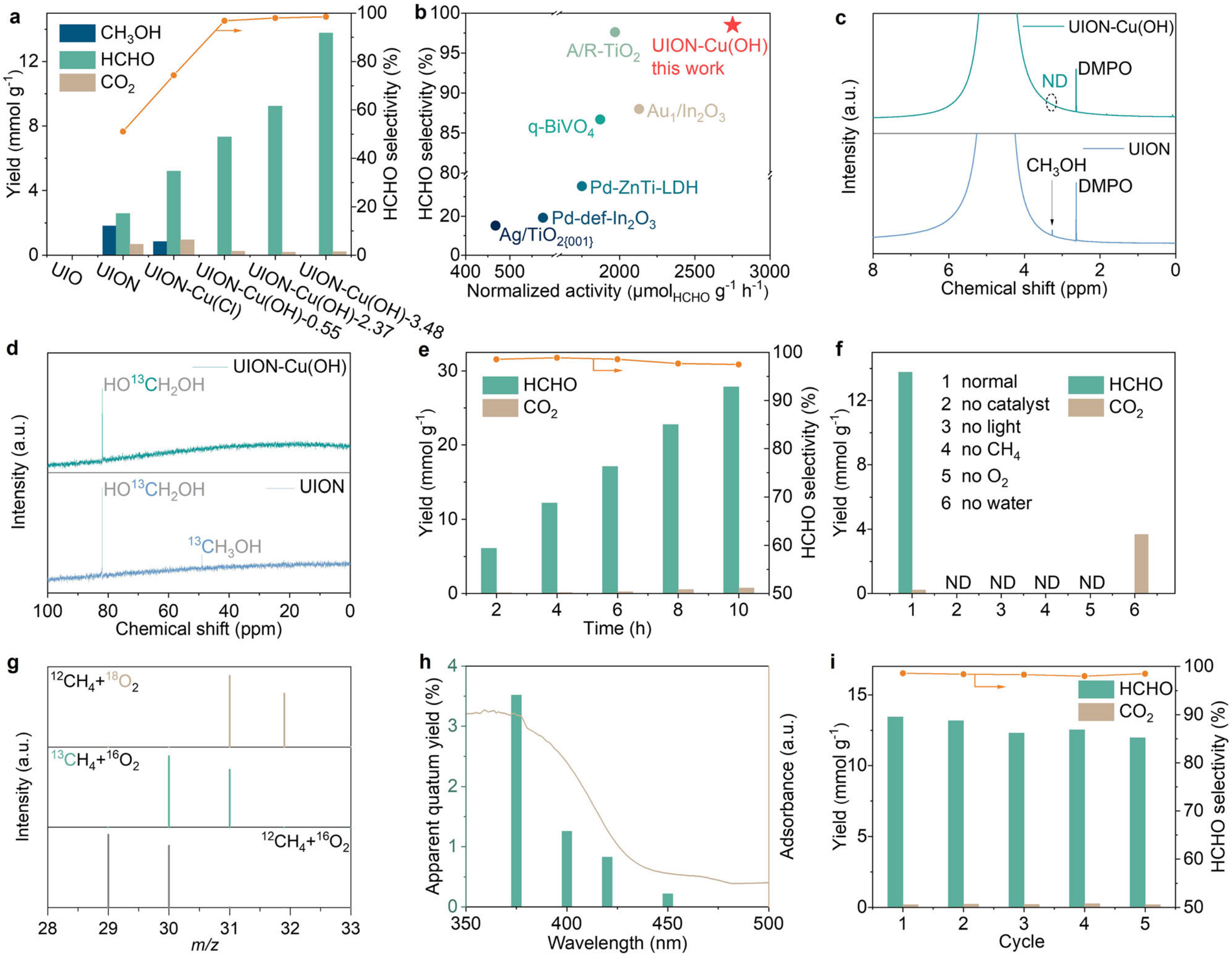

Fig. 3 | Photocatalytic CH_4 conversion performance. **a** Productivity assessments for oxygenated products obtained over UIO, UION, UION-Cu(Cl), and UION-Cu(OH) as the photocatalysts. **b** Comparison of the catalytic activity for selective oxidation of CH_4 to HCHO over UION-Cu(OH) with other photocatalysts[6,16,33–36]. **c** ^{1}H NMR spectra of the photocatalytic products over UION and UION-Cu(OH). **d** ^{13}C NMR spectra of the photocatalytic products over UION and UION-Cu(OH). **e** Time course for HCHO selectivity and product yields over UION-Cu(OH). **f** Photocatalytic activities under different reaction conditions. **g** GC-MS spectra of the produced HCHO with isotopically labeled $H_2^{18}O$, $^{18}O_2$, and $^{13}CH_4$. **h** AQE values at different monochromatic wavelengths along with the diffuse reflectance spectrum of UION-Cu(OH). **i** Cycling tests over UION-Cu(OH) with five-cycle run.

The charge transfer from UION to mono-copper sites is proved by in situ XPS spectra (Fig. 4f). Under light illumination, the XPS characteristic peak of Cu moves toward the low binding energy direction accompanied by the weakening of the Cu^{II} satellite peak, confirming the role of mono-copper site as an electron acceptor in the photocatalytic processes by UION-Cu(OH). In situ EPR spectra of the UION and UION-Cu(OH) are performed to further explore the details of the photoexcitation and charge transfer mechanisms. Under illumination, the EPR signal of UION and UION-Cu(OH) at $g = 2.003$ gradually enhanced, suggesting the generation of photoexcited electrons (Supplementary Fig 33)[39]. By contrast for the UION-Cu(OH) sample, the Cu^{II} EPR signal weakened under the light irradiation, indicating that the content of Cu^{II} species decreased, as the Cu^{I} and Cu^{0} are EPR silent, proving that photogenerated electrons will move and gather to Cu sites (Supplementary Fig 34)[17]. The XAFS test under illumination reveals a consistent trend. As illustrated in Fig. 4g, the Cu k-edge XANES spectra of UION-Cu(OH) under illumination shift towards a lower energy direction, suggesting a decrease in the valence state of the Cu site, confirming the transfer of photogenerated electrons to the mono-copper sites. It is worth noting that the peak intensity in the R-space decreases under illumination (Fig. 4h), suggesting a reduction in the coordination number of the mono-copper site, which may originate from the detachment of -OH groups during the photoactivation process. Hence, further fitting of the data under illumination was conducted (Fig. 4i). The results indicate that the Cu species undergo a transition to tri-oxygen coordination after illumination, exposing the activated mono-copper sites. In summary, the mono-copper site accumulates photogenerated electrons and eliminates coordinated hydroxyl groups, creating an electron-rich exposed atomic active site and serving as a platform for selective methane oxidation.

Mechanistic investigations

The core issue regarding the reaction mechanism is the generation of radicals, which involves the band structure of the photocatalyst and the surface reaction sites. We first determined the bandgap and band positions of the UION-Cu(OH) photocatalyst using UV-VIS DRS and XPS valence band spectra (Supplementary Fig. 35). Given that the valence band and conduction band positions of the UION-Cu(OH) photocatalyst are 2.18 eV and −0.65 eV, respectively, the generated photoinduced carriers can drive the activation of CH_4 and O_2 but cannot convert H_2O into •OH[6,16,40]. Therefore, the activation process of O_2 at the reaction sites determines the final product selectivity. Subsequently, a series of in situ characterizations, including in situ XAFS,

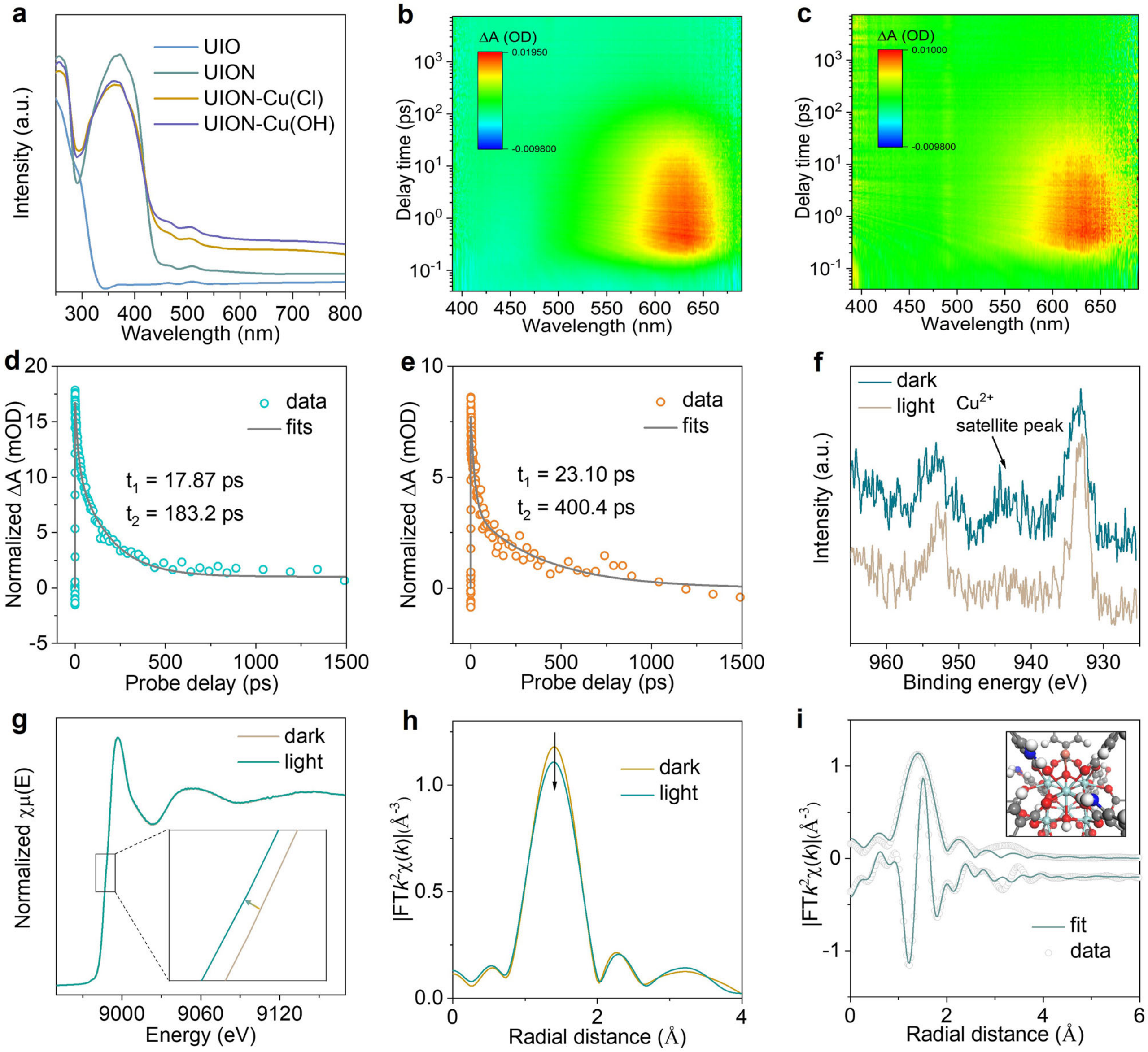

Fig. 4 | Detection of charge dynamics. **a** Diffuse reflectance UV-vis spectra of UIO, UION, UION-Cu(Cl), and UION-Cu(OH). **b**, **c** Transient absorption contour plot of UION (**b**) and UION-Cu(OH) (**c**) under 355 nm pump light. **d**, **e** Transient absorption decay kinetics of UION (**d**) and UION-Cu(OH) (**e**) probed at 625 nm. **f** In situ XPS spectra of UION-Cu(OH) under dark and light irradiation conditions. **g** In situ XANES Cu k-edge spectra of UION-Cu(OH) under dark and light irradiation conditions. **h** Changes in R space of UION-Cu(OH) under dark and light irradiation conditions. **i** Fitting of the EXAFS data under lighting conditions.

in situ EPR, in situ TRPL, and in situ diffuse reflectance infrared Fourier transform spectroscopy (DRIFTS), have been employed to elucidate the evolution of the electronic states at the reaction sites and the surface species during the photocatalytic process.

As shown in Fig. 5a, a shift of the Cu K edge to higher energy levels can be observed as O_2 is introduced under dark condition, indicating the increase in the oxidation state of the Cu species, presumably due to the adsorption of O_2 on the mono-copper site. Upon commencement of illumination, a reversal in the Cu K-edge absorption energy change was noted, suggesting a reduction in the oxidation state of Cu, potentially attributed to the transfer of photogenerated electrons to mono-copper site and the photoreduction of adsorbed O_2. As CH_4 is additionally introduced into the reaction system, a discernible shift in the Cu K-edge absorption energy towards higher values is observed, possibly because the consumption of active oxygen species by CH_4 thus facilitates the adsorption of O_2 onto mono-copper sites. To further elucidate the local coordination structure evolution of the mono-copper active sites during the reaction, the Cu K-edge EXAFS spectra are investigated (Fig. 5b, c and Supplementary Fig. 36). Following the introduction of O_2, the coordination bond length of the Cu site expands, suggesting that the adsorption of O_2 reduces the charge density of the Cu site and weakens the coordination bond. With the introduction of light and CH_4, the bond length gradually recovered, confirming the light-driven reaction between CH_4 and reactive oxygen species.

In situ EPR measurements have also been conducted to unveil the charge transfer behavior during the photocatalytic O_2 activation over UION-Cu(OH) (Supplementary Fig. 37). The Cu^{II} EPR peak displays an evident decrease under light irradiation, and then these EPR signals are partially recovered after the introduction of O_2, clearly revealing that the photogenerated electrons first transfer to the mono-copper site and then migrate to O_2, giving rise to its subsequent reduction[41]. Moreover, the excited-sate lifetimes of pure UION-Cu(OH) and those of UION-Cu(OH) in the presence of O_2, CH_4 or $O_2 + CH_4$ are investigated by TRPL measurements (Supplementary Fig. 38). A decrease in

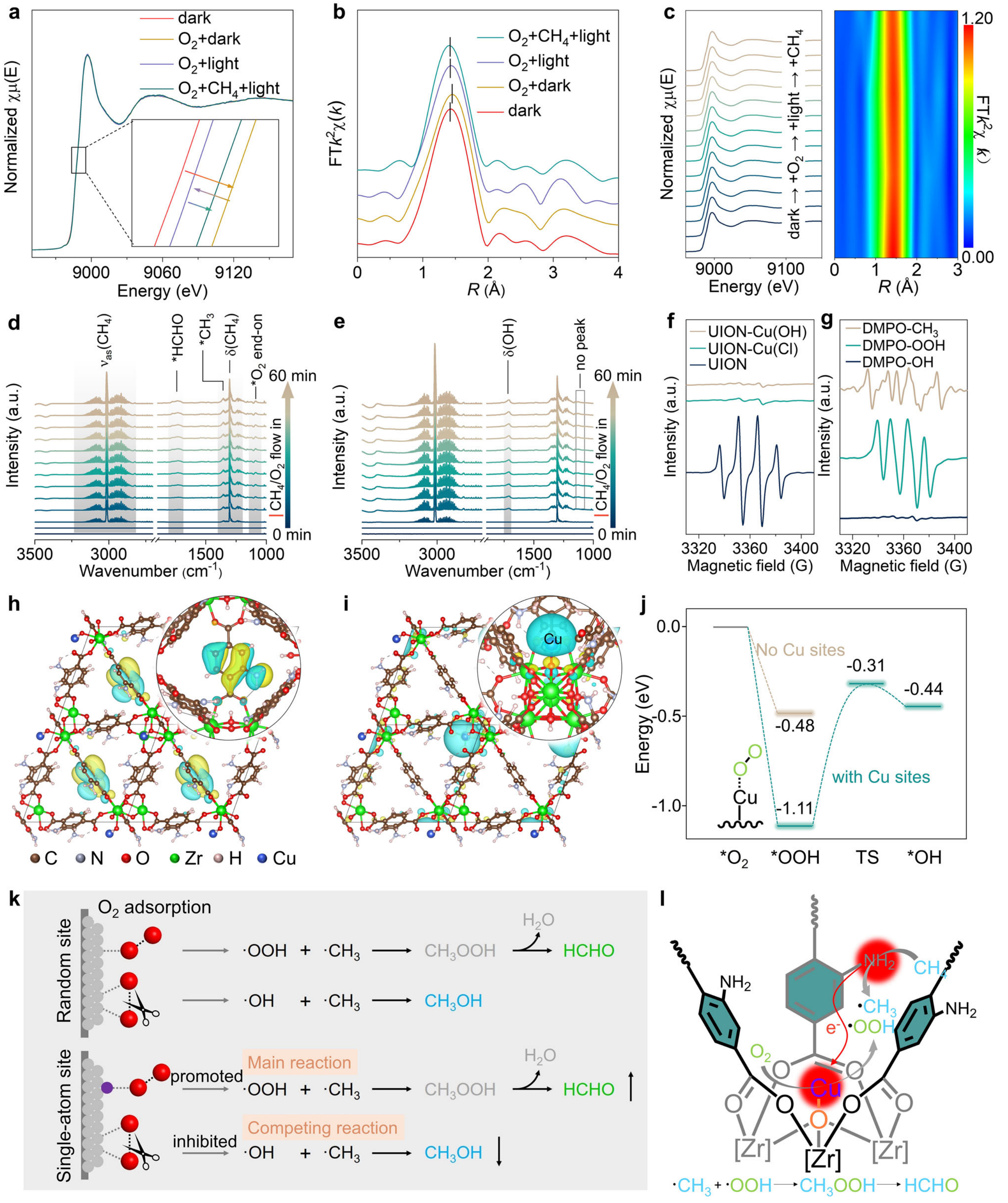

Fig. 5 | Investigation of the active sites and reaction mechanism for the photo-oxidation of CH_4 to HCHO. **a**, **b** In situ XANES Cu k-edge spectra of UION-Cu(OH) photocatalyst treated successively with dark, O_2 + dark, O_2 + light, and O_2 + CH_4 + light condition (**a**) and the corresponding R space spectra (**b**). **c** In situ time-resolved Cu K-edge XANES spectra of the UION-Cu(OH) photocatalyst treated successively with dark, O_2 + dark, O_2 + light, and O_2 + CH_4 + light condition and the corresponding R space spectra. **d**, **e** In situ DRIFTS spectra for CH_4 photo-oxidation over UION-Cu(OH) (**d**) and UION (**e**). **f** EPR spectra of •OH radicals trapped by DMPO over UION, UION-Cu(Cl), and UION-Cu(OH) under light irradiation. **g** EPR spectra of •CH_3, •OOH and •OH radicals trapped by DMPO over UION-Cu(OH) under light irradiation. **h**, **i** DFT calculation of HOMO (**h**) and LUMO (**i**) in UION-Cu, blue and yellow areas represent different spin states. **j** Reaction profiles for activation of O_2 to •OOH or •OH obtained from DFT calculations. **k** The absolute advantage of single-atom sites in the O_2 activation process results in a remarkably selective photo-oxidation of CH_4 to HCHO. **l** Schematic process of charge transfer and photocatalytic CH_4 oxidation reaction over UION-Cu(OH).

the excited-state lifetime of UION-Cu(OH) has been observed with either O_2 or CH_4, suggesting the involvement of both activation of O_2 and CH_4 in the reaction mechanism. Notably, the presence of $O_2 + CH_4$ decreased the excited-state lifetime further, indicating a rapid reaction between the activated species of O_2 and CH_4[42].

Furthermore, in situ DRIFTS measurements have been carried out to investigate the adsorption state of the reactants and reaction intermediates during the reaction process. With the extension of the reaction time, the signals of the reaction intermediate $^*CH_3$ (1356 cm^{-1}) and product *HCHO (1738 cm^{-1}) steadily rise[43,44], and no distinctive peaks related to CH_3OH are detected, which is consistent with the ultra-high HCHO selectivity of UION-Cu(OH) (Fig. 5d). However, a hydroxyl signal possibly attributed to HCHO is observed on UION, corresponding to poor selectivity in the absence of a single copper site (Fig. 5e)[45]. Clearly, both UION and UION-Cu(OH) exhibit distinct CH_4 adsorption and $^*CH_3$ intermediate signals[46]. Given that the linker can enrich photogenerated holes and CH_4 (Supplementary Fig. 39), it can reasonably be speculated that CH_4 undergoes oxidation to form $^*CH_3$ active species through the action of photogenerated holes on the linker. Interestingly, a distinct O_2 end-on adsorption signal (1080 cm^{-1}) is observed on UION-Cu(OH), but this phenomenon is not found on UION[16], suggesting that the difference in product selectivity may arise from a change in the O_2 adsorption state (Supplementary Fig. 40). As distinct modes of O_2 adsorption can influence its reduction process, consequently yielding different types of free radicals to affect the selectivity (Supplementary Fig. 41)[16,25,47], EPR testing has been conducted to confirm the existence of free radicals during the reaction[48,49]. The DMPO-OOH signal displays twice the intensity on UION-Cu(OH) compared to UION, implying that the formation of •OOH is more favorable over the mono-copper site (Supplementary Fig. 42). Contrastingly, the DMPO-OH signal of UION-Cu(OH) almost disappeared after the introduction of mono-copper sites (Fig. 5f). Based on the above in situ analysis, it is determined that O_2 exhibits a preferential activation to form •OOH at mono-copper sites. The copper site has an absolute advantage in competing for O_2, and the rapid O_2 conversion causes near-total inhibition of the reaction at random sites, thus promoting the significant tilt of the competitive equilibrium and resulting in highly selective •OOH generation (Fig. 5k). Therefore, the predominant active species are •OOH and $•CH_3$ in the UION-Cu(OH)-mediated photocatalytic CH_4 oxidation process (Fig. 5g), resulting in the ultra-high selectivity for the production of HCHO.

Drawing from the aforementioned experimental results, the reaction pathway for the highly selective photocatalytic oxidation of methane to formaldehyde on the engineered catalyst can be unequivocally determined. Initially, the UION-Cu(OH) catalyst is excited when exposed to illumination, leading to the migration of photogenerated electrons from the linker to the mono-copper site. Following that, methane is adsorbed by the amino group and subsequently undergoes oxidation and dehydrogenation facilitated by photogenerated holes, leading to the formation of $•CH_3$ (Supplementary Fig. 43a). Simultaneously, the mono-copper site is activated under light irradiation, leading to the removal of the original -OH and providing O_2 adsorption sites. Notably, due to the end-on adsorption of O_2 on the mono-copper site, a highly selective reduction occurs, leading to the formation of •OOH (Supplementary Fig. 43b).

Then, DFT calculations have been conducted to substantiate both the experimental findings and the derived reaction mechanism. In both UION and UION-Cu, the highest occupied molecular orbital (HOMO) is situated on the linker (Fig. 5h and Supplementary Fig. 44a), affirming that the amino group-containing linker serves as the primary excitation region for photoelectrons[50]. However, in contrast to the uniform distribution of the lowest unoccupied molecular orbital (LUMO) across the UION framework (Supplementary Fig. 44b), the LUMO level on UION-Cu is predominantly concentrated on the mono-copper site (Fig. 5i), which strongly indicates that the mono-copper sites function as electron-rich region (Supplementary Fig. 45). Partial density of states calculations provide a more intuitive demonstration of this conclusion, as they reveal that Cu provides the lowest empty orbital just above the Fermi level (Supplementary Fig. 46). To gain further insights into the reaction mechanism at the molecular level, the catalytic processes for methane and oxygen molecule activation were computed. The obtained energy distribution diagrams indicate that the linker with amino groups can facilitate the adsorption of CH_4, with an adsorption energy of −0.22 eV. More importantly, the activation barrier for methane activation to $•CH_3$ on this linker is significantly reduced, being only 0.93 eV, thereby substantially enhancing the activation of CH_4 (Supplementary Fig. 47). On the other hand, the exposed Cu sites serve as open platforms for O_2 adsorption and activation (Supplementary Fig. 48). Calculations indicate that the Cu site significantly promotes the reduction process of O_2 to •OOH. Although the protonation of $^*O_2$ is exothermic on both UION-Cu and UION, the protonation step from O_2 to •OOH on UION-Cu is more thermodynamically and kinetically favorable than on UION, with the Gibbs activation free energies of −1.11 eV and −0.48 eV, respectively (Fig. 5j). Moreover, the •OOH generated at the Cu site needs to overcome a barrier of 0.8 eV to be further reduced to •OH, which directly contributes to the high selectivity of •OOH in the O_2 reduction process. As a result, the generated $•CH_3$ and •OOH swiftly react within the reaction microcavity of the MOF, resulting in the high-selective production of HCHO (Fig. 5l).

Discussion

In summary, we have constructed a model of highly reactive mono-copper sites on the secondary structural units of Zr_6-MOF to precisely tailor the selectivity and reactivity of CH_4 photo-oxidation. The mono-copper sites can efficiently convert O_2 into •OOH, maintaining an absolute advantage in competition with low-active random sites, consequently suppressing the formation of •OH. The •OOH and $•CH_3$ formed in the micro-reaction chamber provided by the MOF combine rapidly to promote reaction efficiency while achieving high HCHO selectivity. Fundamentally, substrate adsorption and radical generation during CH_4 photo-oxidation have been observed through a series of in situ spectroscopy and assigned to the oxidation-reduction active zones integrated in MOF pores. The operando investigations elucidated the highly selective •OOH generation caused by end-on O_2 adsorption at the mono-copper site, thus inducing a highly single CH_4 oxidation pathway. As an outcome, the UION-Cu(OH) exhibited near 100% product selectivity for CH_4 photo-oxidation to HCHO with a rate of 2.75 $mmol\ g_{cat}^{-1}\ h^{-1}$. Our study offers guidance for the selective oxidation of CH_4 to C_1 compounds facilitated by single-atom catalysts and underscores the potential of using MOFs as innovative supports for the design of metal-centered catalysts.

Methods

Chemicals

The following chemicals were purchased and used as-received without further purification. Zirconium tetrachloride ($ZrCl_4$, ≥99.9%, Sigma Aldrich), 2-aminoterephthalic acid (H_2ATA, ≥99%, Sigma Aldrich), 1,4-benzenedicarboxylic acid (≥98%, Sigma Aldrich), copper(II) chloride ($CuCl_2$, ≥99%, Sigma Aldrich), Formic acid (HCOOH, reagent grade, CS Pharm Chemical), n-Butyllithium (n-BuLi, 2.5 M solution in hexanes, Sigma Aldrich), sodium triethylborohydride ($NaEt_3BH$, 0.1 M in tetrahydrofuran solution, Sigma Aldrich), dimethylformamide (DMF, HPLC grade, Sigma Aldrich), tetrahydrofuran (THF, HPLC grade, Sigma Aldrich).

Catalyst preparation

Synthesis of UION. UIO-66-NH_2 (abbreviated as UION) is synthesized via a solvothermal reaction of H_2ATA and $ZrCl_4$ in DMF and water. H_2ATA (0.2 mmol, 36 mg) is dissolved in 1.2 mL DMF containing 0.1 mL of HCOOH in a 15 mL glass vial and kept on stirring for 15 min. In a separate glass vial, $ZrCl_4$ (0.2 mmol, 47 mg) is dissolved in 0.2 mL water and transferred to the vial containing a solution of H_2ATA. The mixture is kept on heating for 12 h at 120 °C. After cooling to room temperature, the light yellow solid is collected via centrifugation, which is washed with DMF, acetone, and ethanol several times. The as-synthesized UiO-66-NH_2 is immersed in the acetone to exchange DMF, followed by drying at 80 °C under vacuum for 12 h. For comparison, UiO-66 (abbreviated as UIO) is synthesized by using 1,4-benzenedicarboxylic acid instead of 2-aminoterephthalic acid, whereas other parameters remain the same.

Synthesis of UION-Cu(Cl). n-BuLi (50 μL, 2.5 M in hexanes) is added to the slurry of UION (20 mg) in 1 mL THF in a 5 mL glass vial, and the mixture is kept for 1 h at room temperature inside the glovebox. The solid is washed with THF several times to remove the excess n-BuLi. A THF solution of $CuCl_2$ (1 mg/mL) is added to the vial, and the mixture is kept overnight at room temperature. The UION-Cu(Cl) is centrifuged out of the suspension, and followed by washing with THF several times. The sample, UION-Cu(Cl), is further dried at 80 °C under vacuum for 12 h.

Synthesis of UION-Cu(OH). A weighted amount of UION-Cu(Cl) (20 mg) is added into an anhydrous THF solution (50 mL) of the reducing agent sodium triethylborohydride ($NaEt_3BH$, 0.1 M, 1 mL). The mixture is stirred for 1 h at room temperature, and the obtained suspension of UION-CuH is separated via centrifugation followed by washing with THF several times. UION-CuH is taken outside of the glovebox and kept in water for 30 min to afford UION-Cu(OH). The obtained sample is dried under vacuum at 80 °C for 12 h. The ratio of Cu to Zr in the sample is determined by ICP-MS.

Characterizations

Powder XRD are characterized by a powder X-ray diffraction instrument (Bruker D8 Advanced A25 diffractometer) with a Cu Kα target ($\lambda = 1.54056$ Å) at 40 kV and 40 mA. FTIR spectra are obtained on a Nicolet iS10 FTIR spectrometer. SEM is performed on an FEI Teneo VS SEM. TEM images are obtained on a Titan ST microscope from Thermo Fisher Scientific. HAADF-STEM and elemental mapping are performed on a Titan Themis Z microscope. XPS measurements are performed on a Thermo Scientific K-Alpha spectrometer with a monochromatic Al Kα X-ray source. EPR measurements are obtained at room temperature using a Bruker EMX-10/12 EPR spectrometer operated in the X-band frequency. The XAFS spectra (Mn K-edge) are collected at the beamline 1W1B of the Beijing Synchrotron Radiation Facility (BSRF, Beijing) in a fluorescence mode at room temperature. The optical absorption properties of the samples are determined using the diffuse reflection method on a UV-visible light near-infrared spectrometer (Lambda 950). Steady-state PL spectra are recorded on a Carry Eclipse fluorescence spectrometer. N_2 adsorption isotherms were operated using a Micromeritics ASAP 2420 at 77 K. CH_4 adsorption isotherms were operated using a Micromeritics ASAP 2420 at 273 K. TRPL decay curves are obtained on FLS980 fluorescence spectrometers. In situ DRIFT spectra measurements are performed on a Nicolet 6700 Harrick spectrometer with an MCT detector.

Femtosecond transient absorption measurement

The fs-TA measurements are conducted using a commercial fs-TA system[51]. A fundamental 800 nm pulse generated by a Coherent Astrella regenerative amplifier served as the pump source. This pulse is used to pump an optical parametric amplifier (Coherent, OperA Solo), producing a frequency-tunable pump beam spanning the visible light region. The pump beam, with a wavelength of 350 nm, is then focused onto the sample. A white-light continuum probe beam is generated by focusing a weaker portion of the fundamental 800 nm beam onto a sapphire window. The sample is positioned at the overlap of the pump beam and the white-light continuum probe beam. All measurements are conducted with samples in water solution using 1 mm quartz cuvettes.

In situ XAFS measurements

The in situ XAFS measurements are collected at the beamline 1W1B of the (BSRF, Beijing) in a fluorescence mode at room temperature. Placing the sample and vacuum-degassed deionized water into the reaction vessel ensures uniform dispersion. Continuously introduce argon gas into the reaction vessel as a protective atmosphere. Collect data separately under dark and illuminated conditions to investigate the activation of mono-copper sites under light exposure. For in-situ testing of methane oxidation, reaction conditions are introduced step by step to study the reaction process. Firstly, subject the sample to thorough illumination in an argon atmosphere to preliminarily activate mono-copper sites. Subsequently, in the absence of light, collect spectroscopic information as the initial state of the reaction. Introduce O_2 into the reaction vessel, stabilize, and collect spectroscopic data to obtain material information during O_2 adsorption. Resume illumination to gather information during O_2 activation. Finally, introduce CH_4 to complete the methane oxidation reaction.

In situ DRIFTS measurements

The in situ DRIFTS measurements were conducted on a Nicolet 6700 IR spectrophotometer (Thermo Scientific) equipped with a Harrick Praying Mantis DRIFTS gas cell. After loading the catalyst and assembling the reaction cell, He gas (20 mL/min) was introduced to purge the system for 30 min to remove air. The background was collected after purging. Subsequently, the catalyst was irradiated using a xenon lamp light source, and infrared spectra collection was initiated. Each spectrum was scanned 32 times at a resolution of 4 cm^{-1}. After collecting spectra for 10 min, a mixed gas of CH_4 and O_2 ($CH_4/O_2 = 1/1$, total flow rate of 20 mL/min) was introduced, and data collection continued for 50 min. Throughout the experiment, the system was temperature-controlled at 20 °C using a recirculating water cooling system to prevent potential hazards.

TRPL measurements

The TRPL spectra were conducted on a FLS980 fluorescence spectrometer. Specifically, the catalyst was dispersed in deionized water and sonicated to form a uniform dispersion (1 mg/mL). Then, 1 mL of the dispersion was placed into a cuvette, excited at 380 nm, and decay transients were recorded at an emission wavelength of 610 nm. For TRPL testing with different atmospheres, the corresponding gas was bubbled through the dispersion until saturation before the test, and the gas was continuously purged over the liquid surface during the test. All other testing conditions remained the same.

EPR measurements

The EPR measurements were carried out at X-band on a Bruker EMX-10/12 EPR spectrometer. For the solid EPR tests, the MOF sample was prepared by loading 25 mg into a J. Young quartz tube (outer diameter, 4 mm; inner diameter, 2.8 mm). The gas in the tube was replaced with Ar, and measurements were taken, including EPR spectra under dark conditions and after 2 min and 5 min of illumination. The EPR spectra under an oxygen atmosphere were measured by replacing Ar with O_2. Additionally, the radical signals were tested in a dispersion system. In these experiments, DMPO was used as the spin-trapping reagent. As a nitrone spin trap, DMPO is widely employed to capture short-lived radicals by forming more stable radicals, thereby generating a significant EPR signal. Specifically, mix 50 μL of the catalyst dispersion (1 mg/mL) with 10 μL of DMPO solution (10%) in the dark. Introduce the reaction gas (O_2 or CH_4) into the system, and then collect in-situ EPR spectra under visible light. For the detection of •OOH, methanol was used as the solvent for the system, while deionized water was used as the solvent for •OH and •CH_3. All reagents and test tubes were deoxygenated with Ar gas before use.

Computational details

The first-principles calculation of spin polarization based on DFT implemented by CP2K/Quickstep package[52] was performed with the plane wave cutoff of 350 Ry. The Gaussian basis set consisting of a double-ζ with one set of polarization functions (DZVP)[53] was used to optimize structures. The Perdew-Burke-Ernzerhof exchange-correlation functional[54] with the approach of Grimme (DFT-D3)[55] was adopted. Due to the large size of the model, single gamma point grid sampling was used. The analysis of the excited state was finished via the Multiwfn code[56].

Data availability

All the data that support the findings of this study are available within the paper and its Supplementary Information files. Source data are provided with this paper.

References

1. Ravi, M., Ranocchiari, M. & van Bokhoven, J. A. The direct catalytic oxidation of methane to methanol—a critical assessment. *Angew. Chem. Int. Ed.* **56**, 16464–16483 (2017).
2. Schwach, P., Pan, X. & Bao, X. Direct conversion of methane to value-added chemicals over heterogeneous catalysts: challenges and prospects. *Chem. Rev.* **117**, 8497–8520 (2017).
3. Gan, Y. et al. Highly selective photocatalytic methane oxidation to methanol using CO_2 as a soft oxidant. *ACS Sustain. Chem. Eng.* **11**, 5537–5546 (2023).
4. Saputera, W. H., Yuniar, G. & Sasongko, D. Light-driven methane conversion: unveiling methanol using a TiO_2/$TiOF_2$ photocatalyst. *RSC Adv.* **14**, 8740–8751 (2024).
5. Luo, L. et al. Water enables mild oxidation of methane to methanol on gold single-atom catalysts. *Nat. Commun.* **12**, 1218 (2021).
6. Fan, Y. et al. Selective photocatalytic oxidation of methane by quantum-sized bismuth vanadate. *Nat. Sustain.* **4**, 509–515 (2021).
7. Sushkevich, V. L., Palagin, D., Ranocchiari, M. & Van Bokhoven, J. A. Selective anaerobic oxidation of methane enables direct synthesis of methanol. *Science* **356**, 523–527 (2017).
8. Ravi, M. et al. Misconceptions and challenges in methane-to-methanol over transition-metal-exchanged zeolites. *Nat. Catal.* **2**, 485–494 (2019).
9. Kwon, Y., Kim, T. Y., Kwon, G., Yi, J. & Lee, H. Selective activation of methane on single-atom catalyst of rhodium dispersed on zirconia for direct conversion. *J. Am. Chem. Soc.* **139**, 17694–17699 (2017).
10. Yuniar, G. et al. Recent advances in photocatalytic oxidation of methane to methanol. *Molecules* **27**, 5496 (2022).
11. Liu, Z. et al. Photocatalytic conversion of methane: current state of the art, challenges, and future perspectives. *ACS Environ. Au* **3**, 252–276 (2023).
12. Li, X., Wang, C. & Tang, J. Methane transformation by photocatalysis. *Nat. Rev. Mater.* **7**, 617–632 (2022).
13. Song, H., Meng, X., Wang, Z.-J., Liu, H. & Ye, J. Solar-energy-mediated methane conversion. *Joule* **3**, 1606–1636 (2019).
14. Song, S. et al. A selective Au-ZnO/TiO_2 hybrid photocatalyst for oxidative coupling of methane to ethane with dioxygen. *Nat. Catal.* **4**, 1032–1042 (2021).
15. Zheng, K. et al. Room-temperature photooxidation of CH_4 to CH_3OH with nearly 100% selectivity over hetero-ZnO/Fe_2O_3 porous nanosheets. *J. Am. Chem. Soc.* **144**, 12357–12366 (2022).
16. Jiang, Y. et al. Enabling specific photocatalytic methane oxidation by controlling free radical type. *J. Am. Chem. Soc.* **145**, 2698–2707 (2023).
17. Luo, L. et al. Nearly 100% selective and visible-light-driven methane conversion to formaldehyde via. single-atom Cu and $W^{\delta+}$. *Nat. Commun.* **14**, 2690 (2023).
18. Song, H. et al. Atomically dispersed nickel anchored on a nitrogen-doped carbon/TiO_2 composite for efficient and selective photocatalytic CH_4 oxidation to oxygenates. *Angew. Chem. Int. Ed.* **135**, e202215057 (2023).
19. Jiang, Y., Fan, Y., Li, S. & Tang, Z. Photocatalytic methane conversion: insight into the mechanism of C(sp^3)-H bond activation. *CCS Chem.* **5**, 30–54 (2023).
20. Li, Q., Ouyang, Y., Li, H., Wang, L. & Zeng, J. Photocatalytic conversion of methane: recent advancements and prospects. *Angew. Chem. Int. Ed.* **134**, e202108069 (2022).
21. An, B. et al. Cooperative copper centres in a metal-organic framework for selective conversion of CO_2 to ethanol. *Nat. Catal.* **2**, 709–717 (2019).
22. Antil, N., Chauhan, M., Akhtar, N., Kalita, R. & Manna, K. Selective methane oxidation to acetic acid using molecular oxygen over a mono-copper hydroxyl catalyst. *J. Am. Chem. Soc.* **145**, 6156–6165 (2023).
23. An, B. et al. Direct photo-oxidation of methane to methanol over a mono-iron hydroxyl site. *Nat. Mater.* **21**, 932–938 (2022).
24. Feng, C., Wu, Z. P., Huang, K. W., Ye, J. & Zhang, H. Surface modification of 2D photocatalysts for solar energy conversion. *Adv. Mater.* **34**, 2200180 (2022).
25. Teng, Z. et al. Atomically dispersed antimony on carbon nitride for the artificial photosynthesis of hydrogen peroxide. *Nat. Catal.* **4**, 374–384 (2021).
26. Garibay, S. J. & Cohen, S. M. Isoreticular synthesis and modification of frameworks with the UiO-66 topology. *Chem. Commun.* **46**, 7700–7702 (2010).
27. Ma, X. et al. Modulating coordination environment of single-atom catalysts and their proximity to photosensitive units for boosting MOF photocatalysis. *J. Am. Chem. Soc.* **143**, 12220–12229 (2021).
28. Dong, J. et al. Continuous electroproduction of formate via CO_2 reduction on local symmetry-broken single-atom catalysts. *Nat. Commun.* **14**, 6849 (2023).
29. He, Y., Li, C., Chen, X.-B., Shi, Z. & Feng, S. Visible-light-responsive UiO-66 (Zr) with defects efficiently promoting photocatalytic CO_2 reduction. *ACS Appl. Mater. Inter.* **14**, 28977–28984 (2022).
30. Han, Y. et al. Control of the pore chemistry in metal-organic frameworks for efficient adsorption of benzene and separation of benzene/cyclohexane. *Chem* **9**, 739–754 (2023).
31. Bruzzese, P. C. et al. 17O-EPR determination of the structure and dynamics of copper single-metal sites in zeolites. *Nat. Commun.* **12**, 4638 (2021).
32. Ikuno, T. et al. Methane oxidation to methanol catalyzed by Cu-oxo clusters stabilized in NU-1000 metal-organic framework. *J. Am. Chem. Soc.* **139**, 10294–10301 (2017).
33. Feng, N. et al. Efficient and selective photocatalytic CH_4 conversion to CH_3OH with O_2 by controlling overoxidation on TiO_2. *Nat. Commun.* **12**, 4652 (2021).
34. Luo, L. et al. Synergy of Pd atoms and oxygen vacancies on In_2O_3 for methane conversion under visible light. *Nat. Commun.* **13**, 2930 (2022).
35. Fu, L. et al. Highly selective conversion of CH_4 to high value-added C_1 oxygenates over Pd loaded ZnTi-LDH. *Adv. Energy Mater.* **13**, 2301118 (2023).
36. Jiang, Y. et al. Elevating photooxidation of methane to formaldehyde via TiO_2 crystal phase engineering. *J. Am. Chem. Soc.* **144**, 15977–15987 (2022).
37. Fu, Y. et al. An amine-functionalized titanium metal-organic framework photocatalyst with visible-light-induced activity for CO_2 reduction. *Angew. Chem. Int. Ed.* **51**, 3364–3367 (2012).

38. Zhang, R. et al. Direct photocatalytic methane oxidation to formaldehyde by N doping Co-decorated mixed crystal TiO_2. *ACS Nano* **18**, 12994–13005 (2024).
39. Tan, H. et al. Photocatalysis of water into hydrogen peroxide over an atomic Ga-N_5 site. *Nat. Synth.* **2**, 557–563 (2023).
40. Amano, F. et al. Photoelectrochemical homocoupling of methane under blue light irradiation. *ACS Energy Lett.* **4**, 502–507 (2019).
41. Li, J. et al. Self-adaptive dual-metal-site pairs in metal-organic frameworks for selective CO_2 photoreduction to CH_4. *Nat. Catal.* **4**, 719–729 (2021).
42. Parvatkar, P. T. et al. A tailored COF for visible-light photosynthesis of 2, 3-dihydrobenzofurans. *J. Am. Chem. Soc.* **145**, 5074–5082 (2023).
43. Bai, S. et al. High-efficiency direct methane conversion to oxygenates on a cerium dioxide nanowires supported rhodium single-atom catalyst. *Nat. Commun.* **11**, 954 (2020).
44. Cheng, Q. et al. Maximizing active Fe species in ZSM-5 zeolite using organic-template-free synthesis for efficient selective methane oxidation. *J. Am. Chem. Soc.* **145**, 5888–5898 (2023).
45. He, Y. et al. In situ identification of reaction intermediates and mechanistic understandings of methane oxidation over hematite: a combined experimental and theoretical study. *J. Am. Chem. Soc.* **142**, 17119–17130 (2020).
46. Li, X. et al. Efficient hole abstraction for highly selective oxidative coupling of methane by Au-sputtered TiO_2 photocatalysts. *Nat. Energy* **8**, 1013–1022 (2023).
47. Zhang, X. et al. Developing Ni single-atom sites in carbon nitride for efficient photocatalytic H_2O_2 production. *Nat. Commun.* **14**, 7115 (2023).
48. Zhou, X.-K., Li, Y., Luo, P.-P. & Lu, T.-B. Synergy of surface phosphates and oxygen vacancies enables efficient photocatalytic methane conversion at room temperature. *ACS Appl. Mater. Inter.* **15**, 36280–36288 (2023).
49. Feng, C. et al. Cooperative tungsten centers in a polymetric carbon nitride for efficient overall photosynthesis of hydrogen peroxide. *Energy Environ. Sci.* **17**, 1520–1530 (2024).
50. Feng, C. et al. Synthesis of leaf-vein-like g-C_3N_4 with tunable band structures and charge transfer properties for selective photocatalytic H_2O_2 evolution. *Adv. Funct. Mater.* **30**, 2001922 (2020).
51. Feng, C. et al. Regulating photocatalytic CO_2 reduction kinetics through modification of surface coordination sphere. *Adv. Funct. Mater.* **34**, 2309761 (2024).
52. VandeVondele, J. et al. Quickstep: fast and accurate density functional calculations using a mixed Gaussian and plane waves approach. *Comput. Phys. Commun.* **167**, 103–128 (2005).
53. VandeVondele, J. & Hutter, J. Gaussian basis sets for accurate calculations on molecular systems in gas and condensed phases. *J. Chem. Phys.* **127**, 114105 (2007).
54. Perdew, J. P., Burke, K. & Ernzerhof, M. Generalized gradient approximation made simple. *Phys. Rev. Lett.* **77**, 3865–3868 (1996).
55. Grimme, S., Antony, J., Ehrlich, S. & Krieg, H. A consistent and accurate ab initio parametrization of density functional dispersion correction (DFT-D) for the 94 elements H-Pu. *J. Chem. Phys.* **132**, 154104 (2010).
56. Lu, T. & Chen, F. Multiwfn: a multifunctional wavefunction analyzer. *J. Comput. Chem.* **33**, 580–592 (2012).

Acknowledgements

This work was supported by King Abdullah University of Science and Technology and Center of Excellence for Renewable Energy and Storage Technologies under award number 5937, the National Key Research and Development Program of China (2022YFE0113800), and the National Natural Science Foundation of China (22122505, 22075250, 21771161).

Author contributions

C.F., M.R., and H.Z. constructed and planned the whole project. C.F. carried out the synthesis of the samples and photocatalytic experiments. S.Z. carried out the XANES and EXAFS characterizations. M.H. performed the EPR tests. Y.R. performed electron microscope imaging. J.L. conducted the DFT calculations. L.X. and C.Z. performed the ultrahigh-resolution HAADF STEM imaging under the guidance of Y.Z. and Y.H. S.W. helped to discuss the reaction mechanism and improve the manuscript. C.F. wrote the manuscript. H.Z. reviewed and edited the manuscript. All authors discussed the results and commented on the manuscript.

Competing interests

The authors declare no competing interests.

Additional information

Supplementary information The online version contains supplementary material available at https://doi.org/10.1038/s41467-024-53483-z.

Correspondence and requests for materials should be addressed to Huabin Zhang.

Peer review information *Nature Communications* thanks Wibawa Hendra Saputera, Hai-Ying Jiang and the other, anonymous, reviewers for their contribution to the peer review of this work. A peer review file is available.